

## Nuclear viscosity of hot rotating $^{224}\text{Th}$

I. Diószegi,<sup>1</sup> N. P. Shaw,<sup>1</sup> I. Mazumdar,<sup>1</sup> A. Hatzikoutelis,<sup>1</sup> and P. Paul<sup>2</sup>

<sup>1</sup>*Department of Physics and Astronomy, State University of New York at Stony Brook, Stony Brook, New York 11794-3800*

<sup>2</sup>*Brookhaven National Laboratory, Upton, New York 11973*

(Received 16 August 1999; published 21 January 2000)

In a detailed investigation of giant dipole resonance (GDR)  $\gamma$ -ray yield from the  $^{16}\text{O}+^{208}\text{Pb}$  system, the absolute  $\gamma$ -ray/fission multiplicities are extracted and reported over a wide range of excitation energy and angular momentum. The enhanced yield of GDR decay  $\gamma$  rays from the compound system has been analyzed within the framework of a modified statistical model containing the nuclear viscosity as a free parameter. The nuclear viscosity parameter  $\gamma$  has been studied over a much wider range of excitation energy and angular momentum than in earlier works. The measured  $\gamma$ -ray multiplicities as well as known neutron multiplicities and evaporation residue cross sections indicate a strongly damped fission motion. The systematics of the extracted dissipation coefficient is fitted equally well with either temperature or a deformation-dependent nuclear viscosity.

PACS number(s): 25.70.Jj, 25.70.Gh, 24.30.Cz

### I. INTRODUCTION

The large scale mass flow across a barrier in a dissipative system is a central topic in contemporary physics [1]. An example of such a phenomenon in nuclear physics is the nuclear fission process. Historically this problem was first addressed by Kramers [2] who studied the role of viscosity in slowing down the diffusion rate in comparison to the decay rate without viscosity as predicted in earlier works of Bohr and Wheeler [3]. A spate of experimental data from heavy-ion-induced nuclear reaction studies, carried out in the last two decades, have rejuvenated interest in nuclear dissipative processes. These experiments have resulted in the interesting observation of unexpectedly large yields of pre-scission charged particles [4], neutrons [5], and giant dipole resonance (GDR) decay  $\gamma$  rays [6] from the compound system prior to fission. The standard statistical model calculation grossly underpredicts the enhanced yields of particles and  $\gamma$  rays. This excess yield of  $\gamma$  rays from heavy compound systems has been analyzed by incorporating the nuclear viscosity parameter for the mass flow and transient effects inside the saddle allowing for the build-up time of the fission flux [7–9]. The viscous diffusion motion reduces the Bohr-Wheeler fission width as it builds up with a characteristic time delay due to the coupling of the collective fission motion to single particle excitations. In addition, the saddle to scission motion is also slowed down due to viscosity resulting in an overall increase in the fission time. This time delay enhances the production of particle and GDR  $\gamma$ -ray decay as the system moves to the saddle point and also from saddle to scission. Therefore, the measurement of pre-fission particle and GDR  $\gamma$ -ray multiplicities provides suitable clocks to probe fission time scale and nuclear viscosity. The results of the neutron data have been summarized by Hilscher and Rossner [10], while Paul and Thoennessen have reviewed the  $\gamma$ -decay results [11].

The present paper follows a line of previous papers devoted to the experimental investigation of fission dynamics in hot rotating nuclei through the GDR  $\gamma$  decay from the fission fragments and the pre-scission compound system [7,8,12]. The conclusions drawn from these works in

$^{16}\text{O}+^{208}\text{Pb}$ ,  $^{32}\text{S}+^{\text{nat}}\text{W}$ , and  $^{32}\text{S}+^{208}\text{Pb}$  systems prompted a systematic measurement of GDR  $\gamma$  rays from these systems over a wider range of excitation energy and angular momentum than reported in previous papers.

Here our primary goal is to investigate the behavior of the nuclear viscosity parameter  $\gamma$  over a relatively large range of bombarding energies and also to study fully its dependence on other observable parameters. The *absolute*  $\gamma$ -ray/fission multiplicity is extracted for the first time for  $^{224}\text{Th}$  and the theoretical spectra are fitted over a range of 2–22 MeV without *any* arbitrary normalization in the low-energy region. This provides a very strong constraint on the set of input parameters for the model used to extract a value for the nuclear dissipation.

An understanding of the temperature dependence of  $\gamma$  is crucial in settling the relative dominance of one-body dissipation [13] and two-body viscosity processes in slowing the fission motion. The previously reported very rapid rise in viscosity (up to  $\gamma \approx 10$  at an excitation energy of  $E_{\text{CN}}^* \approx 84$  MeV) is in qualitative agreement with two-body viscosity process which has a strong dependence on temperature [14]. However, the exact form of temperature dependence of  $\gamma$  within the framework of two-body damping is an open question. The result of previous analyses slightly favored a  $T^2$  dependence over a linear  $T$  dependence [12]. The present experiment, therefore, is aimed at extracting the viscosity parameter  $\gamma$  over a wider range of excitation energy and also to probe any turning over or reduction of  $\gamma$  at higher excitation energy [15], as might be expected for a Fermi liquid.

The organization of the present paper is as follows: the experimental details are presented in Sec. II followed by the experimental results in Sec. III. In Sec. IV we discuss the different aspects of the statistical model code CASCADE including nuclear viscosity and transient effects behind the saddle point. Section V presents a comparison of different theoretical calculations with our experimental results and also with known neutron multiplicities and known evaporation residue cross sections. The calculations are done using different level density approaches, and either temperature or deformation-dependent nuclear viscosity. In Sec. VI we dis-

TABLE I. Summary of the reaction parameters for  $^{16}\text{O}+^{208}\text{Pb}\rightarrow^{224}\text{Th}$  at different beam energies. The columns list the beam energy ( $E_{\text{lab}}$ ), the total fusion cross section ( $\sigma_{\text{tot}}$ ), the excitation energy of the CN ( $E_{\text{CN}}^*$ ), the corresponding maximum ( $l_{\text{max}}$ ) and average ( $l_{\text{ave}}$ ) angular momenta, the average Sierk fission barrier  $\langle B_f \rangle$  at  $l_{\text{ave}}$ , and the initial temperature ( $T_{\text{CN}}$ ) of the CN assuming  $E_{\text{CN}}^* = aT_{\text{CN}}^2$  with  $a=A/9$ . The total fusion cross sections were obtained by extrapolating from the experimental evaporation residue [16,17] and fission cross sections [17,18,19].

$E_{\text{lab}}$ (MeV)	$\sigma_{\text{tot}}$ (mb)	$E_{\text{CN}}^*$ (MeV)	$l_{\text{max}}$ ( $\hbar$ )	$l_{\text{ave}}$ ( $\hbar$ )	$\langle B_f \rangle$ (MeV)	$T_{\text{CN}}$ (MeV)
100	773.9	46.4	37	25.0	4.5	1.37
120	1267.7	64.9	54	36.4	3.4	1.61
140	1585.3	83.5	66	44.5	2.6	1.83
160	1741.5	102.1	75	50.3	1.8	2.03
177	1811.8	117.9	81	54.1	1.3	2.18

discuss the results of these calculation and implications for further investigations. In the appendix we address some questions about the validity of our approximations.

## II. EXPERIMENTAL PROCEDURE

The experimental setup follows that of earlier experiments [8]. A 99.9% isotopically enriched  $980 \mu\text{g}/\text{cm}^2$  thick self-supporting  $^{208}\text{Pb}$  target was bombarded with a pulsed  $^{16}\text{O}$  beam from the Stony Brook Tandem-LINAC facility. The beam pulse repetition time was 106 ns with an average bunch width of  $\sim 800$  ps.

The  $^{224}\text{Th}$  compound nucleus (CN) was formed at five beam energies ranging from 100 to 177 MeV; the relevant reaction parameters are summarized for each bombarding energy in Table I. The  $\gamma$  rays were detected in coincidence with fission fragments in two different detector systems, (1) a large NaI detector and (2) a compact seven element array of  $\text{BaF}_2$  detectors. The experimental configuration is shown in Fig. 1. The target was perpendicular to the beam and the  $\gamma$ -ray detectors were placed at  $\theta_{\text{lab}}=90^\circ$  on opposite sides of the beam axis. The beam current on the target was maintained at around 5 pna for the entire experiment.

The large Stony Brook NaI detector has been described in

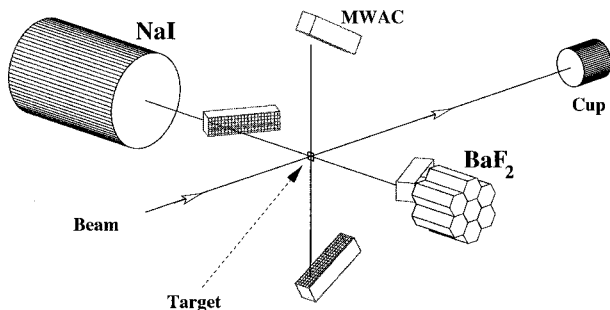


FIG. 1. Schematic diagram of the experimental setup. The seven-element  $\text{BaF}_2$  array and NaI detector are positioned on opposite sides of the beam axis at  $\theta_{\text{lab}}=90^\circ$ , while the four MWAC's are arranged for detection of forward focused fission fragments.

detail elsewhere [20] and only the salient features are mentioned here. The  $25.4 \text{ cm} \times 38.1 \text{ cm}$  cylindrical NaI crystal is surrounded by an annular plastic veto detector and the whole system is inside a 10 cm thick lead shield along with a lead collimator in front of the detector. The detector was placed with the NaI crystal face 60 cm from the target position in order to achieve good neutron- $\gamma$ -ray flight-time separation.

The  $\text{BaF}_2$  array consists of seven hexagonal crystals with an inscribed diameter of 5.6 cm and a length of 14 cm [21]. The superior time resolution of  $\text{BaF}_2$  scintillators allowed the array to be placed 30 cm from the target making the solid angle of the array ( $\sim 0.21$  sr) twice that of the NaI detector. A cooling arrangement maintained the array at a constant temperature of  $\sim 15^\circ\text{C}$  in order to eliminate gain fluctuations due to the well-known temperature dependence of  $\text{BaF}_2$  light output [22,23,24]. In addition the array was frequently calibrated using low-energy  $\gamma$  rays from  $^{88}\text{Y}$  and  $^{228}\text{Th}$ .

The fission fragments were detected in four multiwire avalanche counters (MWAC) arranged in a lamp-shade geometry. This arrangement allows the detection of kinematically coincident fragments, in coincidence with the  $\gamma$ -rays emitted either parallel or perpendicular to the spin axis of the fissioning system. Further details about the geometry, construction, and functioning of the MWAC detectors are provided in Ref. [25].

All analog and timing signals from the  $\gamma$  and fission detectors were digitized using FERA CAMAC modules and recorded event by event. In order to measure absolute  $\gamma$ -ray/fission multiplicities,  $\gamma$ -fission coincidences and down scaled fission single events were recorded. The event trigger was defined in the following manner. Coincidences of any of the  $\gamma$  detectors with any of the MWAC detectors along with scaled-down fission singles events were timed with respect to the radio frequency signal of the accelerator to produce the event trigger. The event trigger started the readout of the digitized detector signals, and also served as a common starting time reference. The FERA TDC's were stopped by the individual detector signals.

For the NaI detector a short (150 ns) and a long (600 ns) integration gate were used, the short gate being placed over the first part of the signal, whereas the long gate integrated the total duration time. In the  $\text{BaF}_2$  detectors individual short (50 ns) and long (1000 ns) gates were also applied. A valid  $\text{BaF}_2$  event was defined when *one* of the seven crystals observed a  $\gamma$  ray above a preset high threshold ( $\sim 2$  MeV), then each of the detector's time and energy signals were recorded. In the off-line analysis, two-dimensional cuts on energy and time of flight were used to discriminate prompt  $\gamma$  rays from fast neutrons. Pileup rejection for both the NaI and the  $\text{BaF}_2$  array was carried out as described in Refs. [21,26] although the granularity of the  $\text{BaF}_2$  array guaranteed that these events were negligible in those detectors. The deposited energy from all  $\text{BaF}_2$  detectors satisfying these cuts were then summed together on an event-by-event basis to create the total  $\text{BaF}_2$  energy spectrum.

Two-dimensional energy versus time-of-flight spectra were created for each of the MWAC detectors to isolate fission fragments from elastically scattered  $^{16}\text{O}$  and recoiling  $^{208}\text{Pb}$  nuclei. Individual fission-gated  $\gamma$ -ray spectra were then

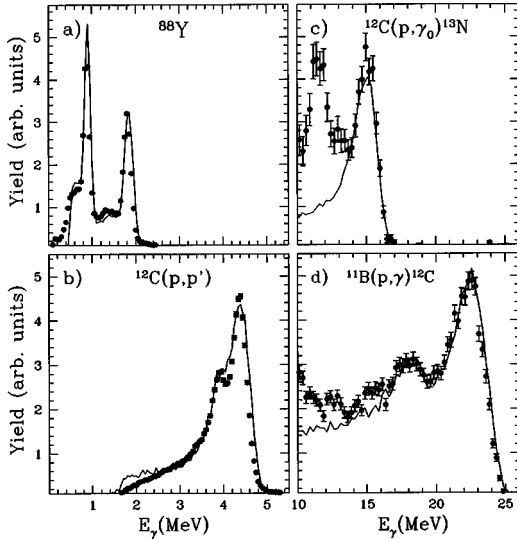


FIG. 2. Experimental spectra for the BaF<sub>2</sub> array compared to results of GEANT simulation (solid line) with a measured resolution of  $\sigma(E_\gamma)/E_\gamma = 0.023 + 0.045/E_\gamma^{1/2}$ . The data are plotted on an arbitrary scale except for the  $^{12}\text{C}(p,\gamma)^{13}\text{N}$  data in panel (c) for which the absolute number of resonant  $\gamma$  rays per incident proton ( $Y_R$ ) is shown in units of  $10^{-12} \epsilon_\gamma dY_R/dE_\gamma (250 \text{ keV})^{-1}$ .

produced for each of the four MWACs in coincidence with either the BaF<sub>2</sub> or the NaI and the thermal neutron background was subtracted. The background contribution was greater for the NaI due to its much larger neutron capture cross section.

An important aspect of the present experiment is the extraction of absolute  $\gamma$ -ray/fission multiplicities [27]. This required a measurement of the energy-dependent line shape and an accurate calculation of the absolute detector efficiencies. The line shape for low  $\gamma$ -ray energies was determined using the radioactive sources  $^{88}\text{Y}$  ( $E_\gamma = 0.898, 1.836 \text{ MeV}$ ) and  $^{228}\text{Th}$  ( $E_\gamma = 2.61 \text{ MeV}$ ). The proton-induced reactions  $^{12}\text{C}(p,\gamma)^{13}\text{N}$  ( $E_\gamma = 4.44, 15.066 \text{ MeV}$ ) with  $E_p = 14.24 \text{ MeV}$  and  $^{11}\text{B}(p,\gamma)^{12}\text{C}$  ( $E_\gamma = 18.12, 22.56 \text{ MeV}$ ) with  $E_p = 7.2 \text{ MeV}$  were used for higher energies. Figure 2 shows the results of these line shape measurements for the BaF<sub>2</sub> array compared to calculations of the Monte Carlo detector simulation code GEANT3 [28] including the full detector and target chamber geometries.

The simulation of the detector system plays a central role in the determination of the  $\gamma$ -ray/fission multiplicities. To prove that the simulation is able to take into account the complicated target geometry, the lead shielding (and collimator for the NaI detector), and the add-back method for the BaF<sub>2</sub> array, the same measurements were used for an efficiency comparison. In the case of the radioactive sources, the known activities were used. For the  $^{12}\text{C}(p,\gamma)^{13}\text{N}$  reaction, the total  $\gamma_0$  resonant thick target yield from the  $J=3/2$ ,  $T=3/2$  resonance was measured with the BaF<sub>2</sub> array to be  $Y_R(\theta=90^\circ) = (2.82 \pm 0.1) \times 10^{-11}$  per incident proton. The known resonance strength of  $Y_R = (6.83 \pm 0.22) \times 10^{-9} \gamma_0$ 's per incident proton at  $\theta_{\text{lab}} = 125^\circ$  and the known angular distribution of  $Y(\theta) = Y_R [1.0 - (0.68 \pm 0.03)P_2(\cos\theta)]$  [29] gives a predicted yield for the BaF<sub>2</sub> array of  $Y_R(\theta=90^\circ)$

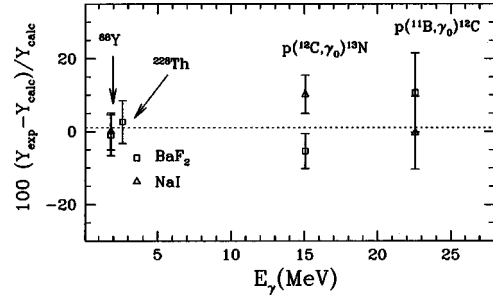


FIG. 3. Percent difference between measured and calculated  $\gamma$ -ray yields for the BaF<sub>2</sub> array (squares) and the NaI detector (triangles).

$= (2.98 \pm 0.1) \times 10^{-11} \gamma_0$ 's per proton, in good agreement with the measured value. A similar comparison was performed for the  $^{11}\text{B}(p,\gamma)^{12}\text{C}$  reaction using a  $760 \mu\text{g}/\text{cm}^2$  thick  $^{11}\text{B}$  target. After measuring the  $\gamma_0$  yield at  $E_\gamma = 22.56 \text{ MeV}$  the target was chemically analyzed and found to contain  $(36 \pm 1)\%$   $^{11}\text{B}$ . The measured  $\gamma_0$  cross section of  $(13.1 \pm 1.1) \mu\text{b}/\text{sr}$  at  $\theta_{\text{lab}} = 90^\circ$  [30] and the measured angular distribution of Ref. [31] were included in a GEANT calculation. The results of these comparisons for the BaF<sub>2</sub> array and the NaI detector are presented in Fig. 3 as the percent difference between the experimental and the calculated yields. The experimental and calculated yields differ by less than 10% over the entire energy range of interest.

These investigations provide confidence that the GEANT simulation of the BaF<sub>2</sub> array and the NaI detector properly describes the experimental setup. A series of GEANT calculations up to  $E_\gamma = 30 \text{ MeV}$  was then performed and used to build the response matrices which were used to fold the theoretical calculations.

The absolute  $\gamma$ -ray multiplicity spectrum for each MWAC was obtained by dividing the measured fission-gated  $\gamma$ -ray spectrum by the total number of measured fission singles. Because the MWAC efficiency enters equally in the  $\gamma$ -fission events and in the fission singles, the multiplicity of  $\gamma$ 's per fission is independent of the MWAC efficiency. The four  $\gamma$ -MWAC multiplicity spectra were then averaged to give the final angle-averaged total multiplicity spectrum. In earlier works [7,8,9,12,20] the theoretical spectra were normalized to the fission gated  $\gamma$ -ray spectra and no absolute multiplicities of  $\gamma$  per fission were reported. This is the first use of absolute  $\gamma$ -ray multiplicities in  $^{16}\text{O} + ^{208}\text{Pb}$  and it eliminates a significant uncertainty in comparing model calculations to the data.

### III. EXPERIMENTAL RESULTS

Figure 4 presents the absolute multiplicity of  $\gamma$  rays per fission for the five beam energies measured, with the BaF<sub>2</sub> and NaI spectra in the left and right panels, respectively. The top panels show that the low-energy ( $E_\gamma \leq 8 \text{ MeV}$ )  $\gamma$ -ray/fission multiplicities increase only modestly with increasing bombarding energy, while the high-energy ( $E_\gamma > 8 \text{ MeV}$ ) yield exhibits a dramatic increase. The NaI spectra at 100, 120, and 140 MeV are also in good agreement with the previously measured data [6,7,8]; the current data, however,

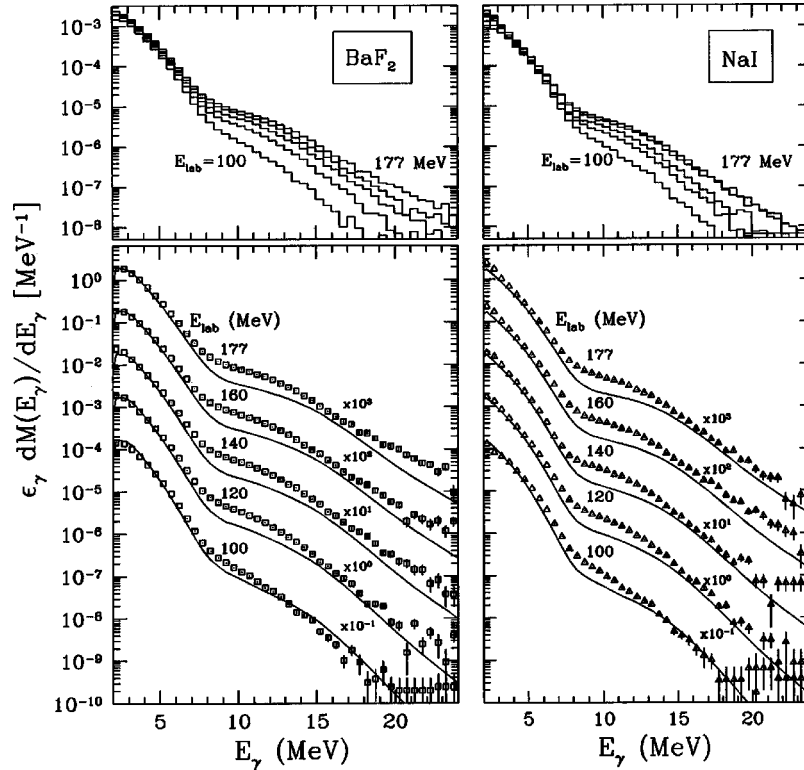


FIG. 4. Top panels:  $^{16}\text{O}+^{208}\text{Pb}$  absolute  $\gamma$ -ray multiplicities measured with the  $\text{BaF}_2$  array and the NaI detector are shown as histograms. Bottom panels: the measured absolute multiplicities (squares for  $\text{BaF}_2$  and triangles for NaI) are compared to CASCADE calculations (solid lines) which do not include nuclear viscosity. The calculated spectra have been folded with the corresponding detector response function.

have a much lower energy threshold and are on an absolute scale. The exponential spectra measured with the two detectors are strikingly similar, proving that the thermal stabilization of the  $\text{BaF}_2$  array combined with frequent energy calibrations satisfactorily overcame the temperature sensitivity of the  $\text{BaF}_2$  crystals.

A “standard” CASCADE calculation folded with the response function of each detector is compared to the data in the bottom part of the figure. The “standard” calculation includes no viscosity and uses the traditional Pühlhofer interpolation [32] for the level densities with Dilg parameters below 7.5 MeV,  $a_{\text{LDM}}=A/9$  in the liquid drop region above 15 MeV, and using a linear interpolation of the parameters between the two regions. A Gaussian mass distribution was used for the fission fragment calculation and the total kinetic energy (TKE) of the fragments was calculated according to the Viola systematics [33] modified for asymmetric mass splits according to Ref. [34]. The Sierk fission barriers [35] were used, scaled by a factor of  $k_f=0.85$  in order to bring the residue cross sections into agreement for the lower bombarding energies, and the level density parameter at the saddle point was set equal to the level density parameter at the equilibrium deformation (i.e.,  $a_f/a_n=1$ ), as in Ref. [12]. The GDR  $\gamma$  decay of fission fragments was assumed to exhaust 100% of the classical sum rule, having a width of 6.5 MeV, and a centroid energy with the systematics of Gaardhøje for giant dipole resonances built on excited states [36].

In agreement with earlier results it is clear that this “stan-

dard” calculation is not able to provide a good fit to the measured spectra. Note that without any normalization the agreement between the  $\gamma$ -ray data and the folded calculation is very good at low energy (3–4 MeV). However, this calculation underestimates the  $\gamma$ -ray yield around 10 MeV (the region of the GDR in the CN system) and again for the higher bombarding energies. The same calculation also drastically underpredicts the precission neutron multiplicities (not shown here) and while it fits the evaporation residue (ER) cross sections reasonably well near the barrier, it nonetheless fails to reproduce the general trend of the residue cross sections with increasing bombarding energy (see Fig. 4 of Ref. [12]).

The strong increase in precission yield of both  $\gamma$  rays and neutrons as a function of beam energy is an indication of an increasingly long-lived compound system which is not accurately modeled by the “standard” calculation. This is the motivation for including dissipative effects in the model, which is discussed in the following section. Since the experimental spectra measured with the  $\text{BaF}_2$  array and the NaI detector are in good agreement and the  $\text{BaF}_2$  data contain superior statistics, further calculations are presented here only with the  $\text{BaF}_2$  spectra.

#### IV. THE MODEL

The analysis of the data was carried out with a modified version of the code CASCADE [7,32]. The code unifies the Hauser-Feshbach formalism of statistical decay of excited

nuclei and the dynamical build up of the fission probability flow over the fission barrier as modeled in the works of Grangé, Weidenmüller, and their collaborators [37–42].

The original CASCADE code, written by Pühlhofer in 1977, is a pure statistical model code. The excited CN is characterized by an initial excitation energy and angular momentum distribution, realized in an  $(E, J)$  matrix. For each matrix element the neutron, proton,  $\alpha$ ,  $\gamma$ , and fission decay probabilities are calculated, and the corresponding population is transferred to new  $(E, J)$  matrices, representing the daughter nuclei. This procedure is continued until the nuclei cool below the particle emission threshold, then finished by calculating the low-energy  $\gamma$ -ray emissions.

The particle decay rates are determined as

$$R_p dE_p = \frac{\rho_f(E_f, J_f)}{h \rho_i(E_i, J_i)} T(E_p) dE_p, \quad (1)$$

where  $\rho_i$  and  $\rho_f$  are the level densities of the initial and final nuclei.  $T(E_p)$  is the transmission coefficient of the particle of energy  $E_p$  carrying the appropriate angular momentum consistent with conservation of total angular momentum. The transmission coefficients are calculated from the optical model.

In this work the optical model parameters of Wilmore and Hodgson [43] were used for the neutron transmission coefficients. This parameter set was measured for 1–5 MeV neutron scattering, which fits well the energy range of the evaporated neutrons in the present reaction. Optical model parameters of Rapaport [44] were measured for neutron energies of 6–26 MeV, and should not be used in this case. For the protons and  $\alpha$  particles the parameters of Perey [45] and Huizenga and Igo [46] were used, respectively.

The rate of  $\gamma$  decay is given by a similar formula:

$$R_\gamma dE_\gamma = \frac{1}{h} \frac{\rho_f(E_f, J_f)}{\rho_i(E_i, J_i)} \sum_L f_L(E_\gamma) E_\gamma^{2L+1} dE_\gamma, \quad (2)$$

where  $L$  denotes the multipolarity of the  $\gamma$  ray. Later versions of CASCADE [20,47] also consider the emission of giant dipole resonance (GDR)  $\gamma$  rays from highly excited states. The decay of such a resonance state can be deduced with the reciprocity theorem using the photon absorption cross section. The absorption cross section for a giant dipole photon for a spherical nucleus is well reproduced by a Lorentzian distribution. The strength function for GDR emission has the form

$$f_{\text{GDR}}(E_\gamma) = 2.09 \times 10^{-5} \frac{NZ}{A} S \frac{\Gamma_{\text{GDR}} E_\gamma}{(E_\gamma^2 - E_{\text{GDR}}^2)^2 + \Gamma_{\text{GDR}}^2 E_\gamma^2}, \quad (3)$$

where  $S$  is the fraction of the classical Thomas-Reiche-Kuhn sum rule [48] which is exhausted by the resonance.

The fission channel was later added to the code by Pühlhofer, calculating the fission using the Bohr-Wheeler formula based upon the saddle-point transition state model [3].

The fission rate is determined by integrating over all available states at the saddle point:

$$R_{\text{fiss}} = \frac{1}{2\pi\hbar\rho_1(E_i, J_i)} \int_0^{E_i - E_b} \rho_2(E_i - E_b - E, J_i) dE, \quad (4)$$

where  $E_b(J_i) = E_{\text{rot}}(J_i) + E_f(J_i)$ ;  $E_{\text{rot}}$  is the rotational energy and  $E_f(J_i)$  is the spin dependent fission barrier,  $\rho_1$  is the level density at the initial state  $(E_i, J_i)$ , whereas  $\rho_2$  is the level density at the saddle point.

The balance between different decay modes of the excited nucleus crucially depends on the nuclear level density of the compound nucleus and its daughters. The particular functional form used in CASCADE for the level density at a fixed excitation energy  $E$  and angular momentum  $J$  is given by

$$\rho(E, J) = \frac{2J+1}{12\theta^{3/2}} \sqrt{a} \frac{\exp(2\sqrt{a}U)}{U^2}. \quad (5)$$

Here  $U = E - \Delta - J(J+1)\hbar^2/2\theta'$  is the internal thermal energy of the system,  $\theta' = \theta(1 + \delta J^2 + \delta' J^4)$  represents the moment of inertia of a deformable rotating liquid drop with small deformability coefficients  $\delta$  and  $\delta'$ , and  $\theta$  is the rigid body moment of inertia.

In CASCADE, as developed in Pühlhofer's original version, the variation of level density with temperature is handled by treating the parameters  $a$  and  $\Delta$  separately in different regions of excitation energy. For  $E < 10$  MeV the parametrization of Dilg *et al.* [49] is used for  $a$  and  $\Delta$ . For  $E > 20$  MeV the nucleus is considered as a liquid drop and the level density parameter  $a = A/K$  is used where the value of  $K$  is handled as a free input parameter. The backshift  $\Delta$  in this high-energy region is calculated as the difference of the calculated (liquid drop model, LDM) and experimentally measured binding energies:  $\Delta = M_{\text{exp}} - M_{\text{LDM}}$ . At high excitation energy the pairing and shell effects are assumed to have vanished leaving a smooth mass dependence of  $a$  and  $\Delta$ . In the intermediate region of  $10 \text{ MeV} < E < 20 \text{ MeV}$  a linear interpolation of  $a$  and  $\Delta$  is carried out between the Dilg and liquid drop model values.

The first major extension of CASCADE was to include  $\gamma$  and particle decay of the fission fragments themselves [50]. In this version the computed fission cross sections were stored, the fission  $Q$  value and total kinetic energy release (TKE) were taken into account, and new CASCADE runs were started to calculate the decay of the fragments. Realistic fission fragment mass distributions were used.

As was shown by Kramers [2], the presence of nuclear viscosity reduces the fission rate, so the full Bohr-Wheeler fission rate as given in Eq. (4) is never attained. The fission width, related to the fission rate by  $\Gamma_f = \hbar R_{\text{fiss}}$  is reduced:

$$\Gamma_f^{\text{Kramers}} = \Gamma_f^{\text{BW}} (\sqrt{1 + \gamma^2} - \gamma), \quad (6)$$

where the dimensionless nuclear viscosity parameter  $\gamma$  determines the extent of the reduction and is related to the reduced dissipation coefficient  $\beta$  by  $\gamma = \beta/2\omega_0$  [38,41] where  $\omega_0$  describes the potential curvature at the saddle point. A common approximation used here takes  $\omega_0 = 10^{21} \text{ s}^{-1}$ .

An additional effect of nuclear viscosity is the transient buildup time of the fission flux moving over the barrier [38]. This build-up of the fission motion with a characteristic time constant  $\tau_f$  has its origin in the coupling of fission motion to nucleonic excitations. While the particle and  $\gamma$ -ray decays of the CN start with their full widths at the moment of CN formation time ( $t=0$ ), the fission decay is hindered and time dependent. The dynamical fission width is parametrized as

$$\Gamma_f(t) = x_h(t) \Gamma_f^{\text{Kramers}}, \quad (7)$$

where

$$x_h(t) = [1 - \exp(-2.3t/\tau_f)] \quad (8)$$

is the fission buildup factor. Semiquantitative analytical expressions for the transient time  $\tau_f$  as the fission width reaches its asymptotic value are given by Refs. [41,42]. For overdamped motion

$$\tau_f = \frac{\beta}{2\omega_1^2} \ln(10B_f/T), \quad (9)$$

where  $\omega_1$  characterizes the frequency inside the barrier,  $B_f$  is the angular momentum dependent fission barrier height, and  $T$  is the nuclear temperature (where the Boltzmann constant is taken as unit). We can approximate again  $\omega_1 = 10^{21} \text{ s}^{-1}$ , and in this case we can describe the system using only one dimensionless parameter  $\gamma = \beta/2\omega_1 = \beta/2\omega_0$ .

Time does not play an explicit role in the original statistical model: decay rates are determined, and the decayed yield is integrated over an infinite time. Since the ratios of the integrated decay yields are identical to those of the decay widths, the integration is not carried out in the calculation, the daughter populations are transferred to the next CASCADE according to the ratios of the decay widths.

The dynamical time concept was introduced to CASCADE in Ref. [7]. The decay rate for each step and each population (representing a given nucleus in the decay chain) is determined by the statistical model. The most probable lifetime of the system is exactly determined by this decay rate. Therefore for the dynamical time step the most probable lifetime of that given population was chosen. Since neutron emission is the dominant decay channel, the neutron lifetime has been used to describe the time evolution. The time step is calculated from the neutron decay for each decaying nucleus, and the elapsed time is then stored. It was later shown in Ref. [51,52], that other, slightly different time step concepts can also be introduced.

Having introduced the dynamical time into the calculation the time-dependent fission width is calculated at each decay step, and at the stationary limit the Kramers fission widths are used. In this extended code the decay occurring between the saddle and scission points was included. The presence of viscosity will also slow down the fission motion along the saddle to scission path and the saddle to scission time is given as [53]

$$\tau_{\text{ssc}} = \tau_{\text{ssc}}^0 (\sqrt{1 + \gamma^2} + \gamma). \quad (10)$$

$\tau_{\text{ssc}}^0$  is the time constant without dissipation and following Nix [54] is estimated to be  $3.0 \times 10^{-21} \text{ s}$  for  $^{224}\text{Th}$ . Whereas the CN and also the fission fragments have no time limit for their decay, the saddle to scission decay is limited to the saddle to scission time according to Eq. (10).

Due to the higher excitation energies exhibited in our experimental data computational improvements were necessary. We also took advantage of the higher speed and memory capacity of present day computers. These changes included extension of the  $(E,J)$  matrix sizes, improved handling of the level densities and book-keeping. In the previous papers [7,8,12] the  $\tau_f$  delay time was calculated only for the average angular momentum and the initial temperature  $T$  of the system. In the present code we introduced an angular momentum and temperature-dependent delay time  $\tau_f(J,T)$  by calculating the temperature for each  $(E,J)$  matrix element.

In Ref. [12] a temperature dependence of the nuclear viscosity has been observed. The approach used, however, was internally inconsistent, because the viscosity parameter, although depending on the initial excitation energy, was kept constant during the entire deexcitation process, as the system decays from the initial CN to the Yrast states or fissions. To handle this quantity accurately in the present code we introduce the viscosity parameter  $\gamma$  as a temperature-dependent quantity  $\gamma(T)$ , and the temperature dependence is properly taken into account during the cooling process. The temperature dependence of  $\gamma$  is an input function in the present version.

The fission barrier in highly fissile, hot systems can be less than the temperature  $T$  for the higher angular momenta and a fast fission process takes over. It was shown by Weidenmüller and Jing-Shang [39] and further discussed by Grangé [40] that in this case the entire fission process is governed by transients, and the stationary probability flow over the barrier may never be reached. Then the Kramers formula, Eq. (6), becomes meaningless and the buildup time constant  $\tau_f$  characterizes the presaddle lifetime. In fast fission the fully equilibrated CN is formed. However, because of the small barrier and high temperature the average time to reach the saddle-point configuration is much shorter than the neutron or  $\gamma$  lifetime and the fission decay rate greatly exceeds other decay rates. Therefore, the particle and  $\gamma$ -ray emission take place during the saddle to scission motion. (In case of vanishing fission barrier, naturally, the system is formed right at the saddle point.) The viscosity in the fast fission process still affects the saddle to scission time according to Eq. (10). Although the saddle point is passed and the decision to fission is made very quickly, the total time to reach the scission point still can be long due to the large viscosity.

In our calculations we introduced the fast fission process in the following manner. For each  $(E,J)$  matrix element we calculate the temperature  $T$  and the fission barrier  $B_f$ . When  $B_f/T < k$ , where  $k$  is an input parameter for the calculation, particle and  $\gamma$  decay are not allowed. Instead, this population is transferred to the saddle point and will undergo only the saddle to scission decay. Although the choice of  $k$  is some-

what arbitrary,  $k=0.5$  was chosen, for which according to Weidenmüller and Jing-Shang [39] the transients have become dominant.

An effort to simultaneously fit pre- and postscission neutron multiplicities,  $\gamma$ -ray multiplicities, and evaporation residue cross sections revealed problems related to CASCADE's level density interpolation method discussed above. Similar difficulties were previously noted by Kicińska-Habior *et al.* [55,56] in fitting GDR  $\gamma$ -ray spectra from nuclei in the  $A=60$  region.

An alternative approach to this interpolation method was suggested by Ignatyuk *et al.* [57] who proposed a form which reflects the nuclear shell structure at low excitation energy and goes smoothly to the liquid drop behavior expected at high excitation energy. In the backshifted Fermi-gas model, the shell structure makes its appearance through the level density parameter. In Ignatyuk's approach the level density parameter is itself taken as a smooth function of mass but with an energy-dependent factor which introduces the shell structure explicitly:

$$a(U) = \bar{a} \left( 1 + \frac{f(U)}{U} \delta W \right), \quad (11)$$

$$f(U) = 1 - \exp(-U/E_D),$$

where  $U$  is the thermal energy of the CN,  $\bar{a}$  is the asymptotic (or liquid drop) level density parameter,  $E_D$  determines the rate at which the shell effects melt away, and  $\delta W$  is the shell correction taken from the difference between the experimental and LDM masses, ( $\delta W = M_{\text{exp}} - M_{\text{LDM}}$ ).

One implementation of Ignatyuk's basic approach was proposed by Reisdorf [58] and has been favored by numerous authors. It has as its primary contribution a formula for the asymptotic level density parameter reminiscent of liquid drop mass calculations:

$$\bar{a} = 0.04543r_0^3 A + 0.1355r_0^2 A^{2/3} B_s + 0.1426r_0 A^{1/3} B_k, \quad (12)$$

where  $A$  is the nuclear mass,  $r_0$  is the nuclear radius, and  $B_s$  and  $B_k$  are the surface and curvature terms of the liquid drop model, respectively [58]. The pairing energy is given as  $\Delta = \chi(p/A^{1/2})$  where  $\chi = +1, -1, 0$  for even-even, odd-odd, and odd nuclei, respectively. A fit to the available  $s$ -wave resonance neutron spacings resulted in the values  $r_0 = 1.153 \pm 0.01$  fm,  $p = 10.5 \pm 2$  MeV and  $E_D = 18.5$  MeV.

Equation (12) is especially appropriate for fusion-fission reaction calculations because of the explicit dependence of the level density parameter on the nuclear shape. Hasse [59] gives an expansion for the shape dependences,  $B_s$  and  $B_k$ , as a function of nuclear deformation which has now been implemented as an option in CASCADE. (Alternatively, Myers and Swiatecki [60] give a tabulation of  $B_s$  and  $B_k$  as a function of fissility which gives an equivalent result.) The specific application in this case is a calculation of the saddle point level density parameter ( $a_f$ ) which is entirely consistent with the level density parameter at the equilibrium deformation ( $a_n$ ). Calculating the saddle point level density

parameter in this way is in agreement with Charity's statement [61] that temperature-dependent barriers should not be used in statistical model calculations.

An additional complication in handling level density calculations has to do with the temperature dependence of the level density parameter. While the Ignatyuk-Reisdorf method described above has some temperature dependence, it is relatively weak since it merely accounts for the smoothing away of the nuclear shell structure. For example in  $^{224}\text{Th}$ , which has a shell correction of  $\delta W = 1.45$  MeV, the level density parameter changes by only 7% from  $T=0$  MeV ( $a=A/9.8$ ) to  $T=2$  MeV ( $a=A/10.5$ ). Thomas-Fermi calculations, however, indicate that the temperature dependence may be much stronger in reality when effects related to the finite size of the nucleus, the continuum states, shell effects, the momentum and frequency dependence of the effective mass and the variation of these effects with temperature are taken into account. One much cited work is that of Shlomo and Natowitz [62] in which their model (described in Ref. [63]) was utilized to calculate the temperature dependence of the level density parameter. While the basic model has seen many refinements in recent years [64,65], Fig. 1 of Ref. [62] provides guidance about the temperature dependence of nuclear level densities. For  $A=210$ , an increase of roughly 20% is indicated for the inverse level density parameter,  $K=A/a$ , which is significantly larger than the modest temperature dependence already included in Eq. (11).

Thus an additional temperature dependent factor which retains the good agreement with low-energy level density data was included as an option in CASCADE. The final form of the level density parameter is then

$$a(T) = a(U)[1 - \kappa f(T)], \quad (13)$$

$$f(T) = 1 - \exp[-(TA^{1/3}/21)^2],$$

where  $a(U)$  is calculated according to Eq. (11) and  $\kappa$  determines the strength of the additional temperature dependence. This function is drawn from expressions for the temperature dependence of the mean-field parameters in Ref. [62]; a strength of  $\kappa=0.4$  provides a reasonable fit to the curves in Fig. 1 of that work (see also Ref. [66]).

## V. ANALYSIS

### A. Traditional level density approach with nuclear viscosity

It was shown in Fig. 4 that a CASCADE calculation without nuclear viscosity fails to fit the  $\gamma$ -ray multiplicities. As a next step, similar to the previous works [7,8], we included nuclear viscosity. As an example, a calculation for the 120 MeV data is compared to the measured  $\gamma$ -ray multiplicity spectra in Fig. 5. In order to emphasize the excess pre-scission yield in the experimental data, a linear "divided" spectrum is also provided, where the excess of the total experimental or calculated  $\gamma$  spectrum compared to the calculated fission fragment  $\gamma$  yield divided by the same calculated fragment  $\gamma$ -ray contribution. We plot  $(M_\gamma^{\text{total}} - M_\gamma^{\text{post}})/M_\gamma^{\text{post}}$ , where  $M_\gamma^{\text{total}}$  is the measured absolute  $\gamma$ -ray/fission multiplicity and  $M_\gamma^{\text{post}}$  is the calculated postscission  $\gamma$ -ray/fission multiplicity. While

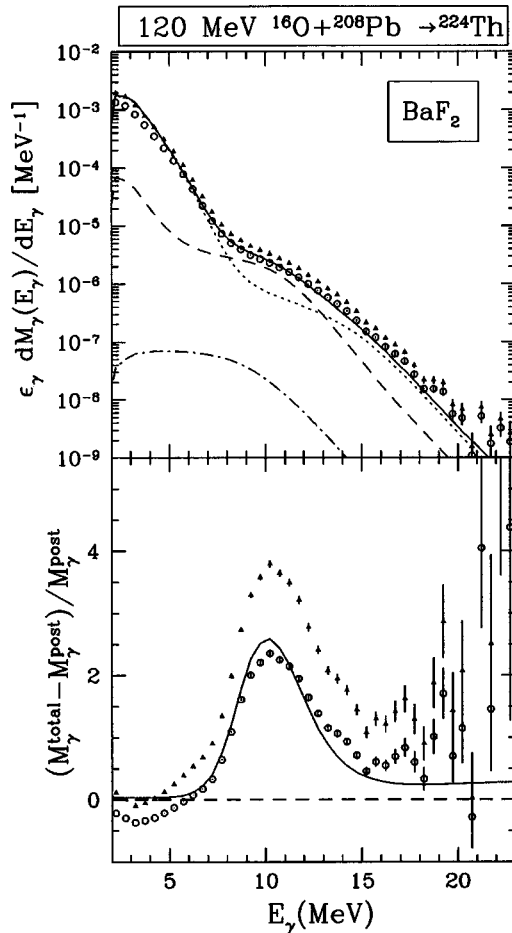


FIG. 5.  $\gamma$ -ray multiplicities for 120 MeV  $^{16}\text{O}+^{208}\text{Pb}$  compared to a calculation with Pühlhofer's level density interpolation method, now including viscosity ( $\gamma=6$ ). The upper panels show the various calculated statistical  $\gamma$ -ray components: presaddle (dashed), saddle to scission (dotted-dashed), postscission (dotted), and total (solid). The lower panels display a comparison in the more sensitive divided representation (see text). The experimental multiplicities in excess of the calculated fission fragment yield are shown on the absolute scale (triangles), while the calculated excess over the fragment yield is plotted as solid line (see text). A scaling factor of 0.7 (circles) is required for experimental points to achieve agreement with the calculations.

this representation is model dependent, it provides a sensitive scale to see even minor disagreements between the data and the theoretical calculation that would otherwise not be apparent from the strongly exponential spectra.

The input parameters for this calculation were similar to that of Ref. [12]: a temperature-independent viscosity of  $\gamma=6$  was included, the Sierk barrier was scaled by a factor of  $k_f=0.73$ , and  $a_f/a_n=1$ . The high-energy CN level density parameter was  $a_{\text{LDM}}=A/8.8$  and for the fragments,  $a_{\text{LDM}}=A/9$ . The GDR parameters for the CN, saddle to scission, and fragments are shown in Table II.

On an absolute scale, this calculation fails to agree with the absolute experimental data except for  $E_\gamma \leq 5$  MeV. Normalizing the calculation to the data improves the agreement substantially although the present low-threshold ( $E_{\gamma,\text{thres}}$

TABLE II. GDR parameters for each stage of the CASCADE calculation: compound nucleus (CN), saddle to scission (SSC), fission fragments (FF). A positive (negative) deformation parameter indicates a prolate (noncollective oblate) deformation. The GDR centroid is 11.5 MeV for both the CN and SSC decay.

System	$\beta$	$E_1$ (MeV)	$\Gamma_1$ (MeV)	$E_2$ (MeV)	$\Gamma_2$ (MeV)
CN	-0.1	11.2	4.5	12.2	5.3
SSC	+0.3	9.7	4.5	12.4	7.3
FF	0.0	Ref. [36]	6.5		

$\approx 2.5$  MeV) data reveal that the calculated curve then crosses the data at low energy. This shows that the free choice of normalization can affect the comparison in an arbitrary way.

To further extend our investigation we also compared the available precission neutron emission [67] and evaporation residue (ER) cross section [16,17] data to the calculations. The “standard” calculation underpredicts the precission neutron multiplicities and ER cross sections. With the introduction of the nuclear viscosity the precission neutron multiplicities rise from  $\nu_{\text{pre}}=0.64$  to 2.17, but are still low by about one neutron. On the other hand, the predicted ER cross section becomes much too large, increasing from  $\sigma_{\text{ER}}=1.5\text{--}60$  mb, whereas the measured value is  $\approx 10$  mb.

Since evaporation residues are highly sensitive to the decay of the excited compound system from the initial steps all the way down to the ground state, the disproportionate increase of the ER cross sections relative to the  $\gamma$ -ray and neutron multiplicities prompted a closer examination of the decay process. Figure 6 displays the neutron,  $\gamma$ , and fission decay widths as a function of time as well as the excitation energy of the system and the population transferred to subsequent daughter nuclei, as calculated by CASCADE. The circles correspond to the calculation of Fig. 5, where Pühlhofer's original interpolation method (Method A) was used in the level density calculation. Results of the alternative procedure (Method B), using the Ignatyuk-Reisdorf formula (11), are plotted as squares. An unusual kink appears in the widths of the Method A calculation at  $\sim 2 \times 10^{-18}$  s, where the neutron width increases suddenly and the system cools off much more quickly in one step than is consistent with previous steps. This occurs around  $E^*=20$  MeV which is suspiciously near the interpolation region used for the level density handling. It has been noted in the literature that Method A can have undesirable consequences [55,56] and a plot of the spin-integrated nuclear level density along with the neutron and fission widths as a function of excitation energy in Fig. 5 is revealing. While the neutron and  $\gamma$  widths unexpectedly increase near the interpolation region (Method A), the fission width actually drops, thus explaining the overestimated residue cross sections relative to the neutron and  $\gamma$ -ray multiplicities.

Thus, the interpolation method of Pühlhofer has intrinsic deficiencies for a fusion-fission reaction. The discontinuities in the nuclear level density caused by the change of slope at the interpolation region result in a large overprediction of the ER cross sections. In previous works on  $^{224}\text{Th}$ , this resulted



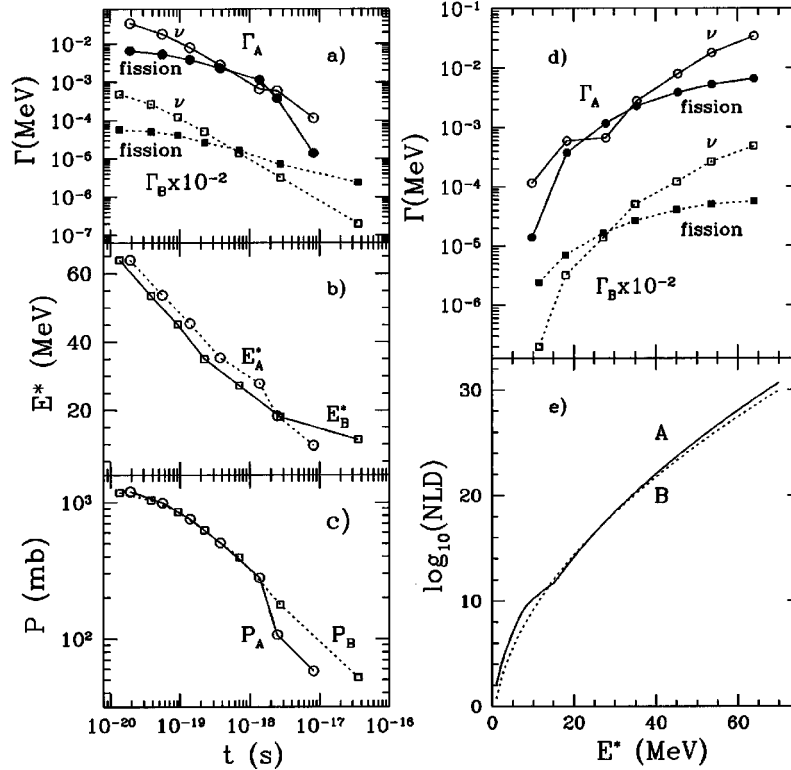


FIG. 6. Various CASCADE quantities from the calculation shown in Fig. 5, and the same using the Ignatyuk-Reisdorf level density formula. The squares are calculations with the CASCADE default level density formalism (Method A), whereas the circles are calculated with the Ignatyuk-Reisdorf level density formula (Method B). Panel (a) displays the average neutron ( $\nu$ ) and fission widths, panels (b) and (c) show the average  $E^*$  and population of the daughter nuclei, respectively, as a function of time. Panel (d) contains the widths of panel (a), but now as a function of excitation energy, and panel (e) the spin-integrated nuclear level density for  $^{224}\text{Th}$ . Note the strong effects in the interpolation region between 7.5 and 15 MeV for the A calculation.

in the need for a drastic scaling of the Sierk barriers (ranging from  $k_f=0.89$  to 0.66), with the additional consequence that the precission neutron multiplicities could not be fitted simultaneously with the ER cross sections. Additionally, the low-energy  $\gamma$ -ray yield was underpredicted, which had not been noticed in previous studies of  $^{224}\text{Th}$  due to the arbitrary normalization of the data to the calculations [68]. Therefore, we implemented the Ignatyuk-Reisdorf level density prescription (Method B) in our code, as described in Sec. IV. Figure 6 demonstrates that the discontinuities that result from the interpolation method are not present when using the Ignatyuk-Reisdorf approach.

### B. Ignatyuk-Reisdorf approach with temperature-dependent nuclear viscosity

A series of calculations using this Ignatyuk-Reisdorf method [Eq. (11)], without the additional temperature dependence of Eq. (13), now for all the available observables is shown in Fig. 7. Here the nuclear radius parameter [which is used in calculating the level density parameter according to Eq. (12)] was set to the default value of  $r_0=1.153$  along with the other default parameters of Ref. [58]. For the fission fragments, the radius parameter was set to  $r_0=1.10$  which is in agreement with the work of Kicińska-Habior *et al.* [55,56] for lighter mass nuclei. In the present work this value of the radius parameter also provides a superior fit to the low-

energy ( $E_\gamma < 8$  MeV) fission fragment  $\gamma$  rays. The full Sierk fission barriers were used. The work of Bolsterli *et al.* [69] based on the liquid drop model provides an estimated saddle-point deformation of  $\beta=0.88$  for a fissility of  $x=0.763$  (for zero angular momentum). The evaporation residues are produced at low angular momenta; therefore to produce a good fit for the residues we used this zero angular momentum saddle-point deformation in calculating the saddle-point level density parameter according to Eq. (12). This corresponds to  $a_f/a_n=1.04$ . Since particle and  $\gamma$  spectra are less sensitive to  $a_f/a_n$ , the same saddle-point level deformation was used for higher angular momenta, and also for the saddle to scission decay. For high CN angular momenta the saddle-point deformation can be much smaller, but the deformation will increase during the saddle to scission decay, so  $\beta=0.88$  reflects the large average deformation during the saddle to scission decay.

For the neutron multiplicities and ER cross sections, the curves show calculated results as a function of bombarding energy, obtained with fixed viscosity of different given strength for each bombarding energy. The plotted  $\gamma$ -ray spectra were then calculated with the viscosity value ( $\gamma_{\text{fit}}$ ) that most closely predicts the precission neutron multiplicity at that beam energy.

Several interesting conclusions can be drawn from an inspection of Fig. 7. The first is the observation that, for all

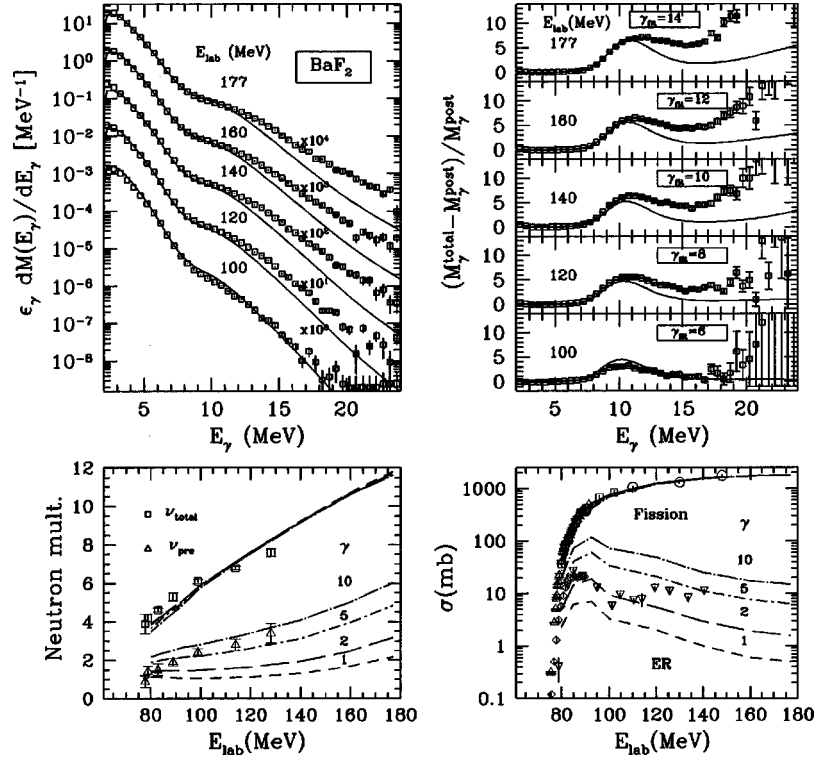


FIG. 7. All available experimental observables for  $^{16}\text{O}+^{208}\text{Pb}\rightarrow^{224}\text{Th}$  compared to calculations using the Ignatyuk-Reisdorf level density prescription combined with constant viscosities indicated. The upper panels display the  $\gamma$ -ray multiplicities (measured with the  $\text{BaF}_2$  array) in both the full and divided representation. For each bombarding energy the viscosity which gave the best fit to both the  $\gamma$ -ray and neutron multiplicities was used. Four curves from calculations with constant  $\gamma=1$  (short dashed), 2 (long dashed), 5 (dotted-short dashed), and 10 (dotted-long dashed) are compared to the experimental neutron multiplicities [67], fission cross sections [17–19], and ER cross sections [16,17] in the bottom panels.

bombarding energies, the absolute multiplicity of  $\gamma$  rays is very well fitted for energies below 10 MeV where the previous method failed to reproduce both the slope as well as the absolute multiplicities. The second conclusion regarding the  $\gamma$ -ray spectra is the increasing (with the bombarding energy) disagreement between the experimental and calculated high-energy tail. This will be a topic of further discussion.

The third conclusion is that a constant viscosity of a given strength is unable to describe all of the experimental observables within the present assumptions; the nuclear viscosity clearly changes with temperature. This can be seen in both the pre-scission multiplicities and the ER cross sections where the experimental data crosses the lines of constant viscosity with increasing bombarding energy. It is also interesting that a much smaller viscosity parameter is required to fit the ER cross sections at a given bombarding energy compared to the multiplicities of either  $\gamma$  rays or pre-scission neutrons. For instance, at  $E_{\text{lab}}=120$  MeV, the pre-scission neutron multiplicity yields  $\gamma_{\text{fit}}\sim 7-8$ . But for the ER cross section at the same bombarding energy, the data clearly indicate a viscosity  $\gamma_{\text{fit}}\leq 5$ .

The top panel of Fig. 8 shows the viscosity values  $\gamma_{\text{fit}}$  extracted from the neutron and  $\gamma$ -ray multiplicities, plotted as a function of the initial CN temperature. The two curves compared to  $\gamma_{\text{fit}}$  are

$$\gamma = 0.2 + 5T, \quad (14)$$

and

$$\gamma = 0.2 + 3T^2, \quad (15)$$

where  $\gamma=0.2$  is assumed [70,71] for  $T=0$ .

These functions were used in the next series of CASCADE calculations, i.e., the initial  $\gamma$  is replaced by the corresponding temperature-dependent  $\gamma$  in each stage of the cooling process. The results are compared to the experimental neutron multiplicities and ER cross sections in the bottom panels of Fig. 8. The calculated  $\gamma$ -ray spectra (not shown here) are virtually unchanged from Fig. 7 since the initial viscosity obtained from these functions is similar to the earlier extracted  $\gamma_{\text{fit}}$ , the calculated high-energy  $\gamma$ -ray tail is still underpredicted. High-energy  $\gamma$  rays come primarily from the CN in the first few decay steps and thus are only sensitive to the viscosity at the initial temperature.

As can be seen in Fig. 8, the agreement with the neutron multiplicities is comparable using either function although the linear form slightly overestimates the pre-scission multiplicities at the lower bombarding energies. The ER cross sections, on the other hand, are definitely better described with the  $T^2$  dependence, as the linear function overpredicts the ER data at all but the highest energy. This may be because the ER cross sections are sensitive to the nuclear viscosity at a much later stage in the decay process than the neutron or  $\gamma$ -ray multiplicities.

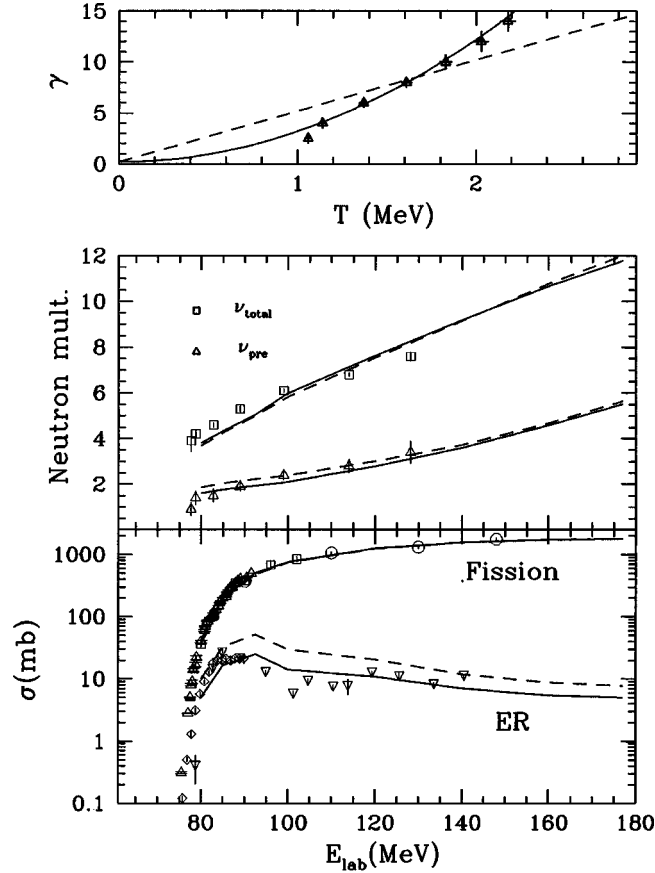


FIG. 8. The upper panel shows the fitted viscosity values extracted from Fig. 7 plotted as a function of the initial temperature of the CN. A linear fit with  $\gamma=0.2+5T$  (dashed line) and a quadratic fit with  $\gamma=0.2+3T^2$  (solid line) are also shown. The lower panels display the results of CASCADE calculations for neutron multiplicities, ER's, and fission cross sections, using both the linear (dashed) and the quadratic (solid) fits for the nuclear viscosity.

The good fits to the ER and neutron spectra are encouraging and justify the soundness of the model in correctly reproducing the decay cascade. However, the agreement with the  $\gamma$ -ray multiplicities for  $E_\gamma > 10$  MeV (i.e., above the GDR peak) is poor, except for the lowest bombarding energy: the high-energy ( $E_\gamma > 10$  MeV) tail was underpredicted by the calculations.

We will now discuss how to improve the agreement of the high-energy  $\gamma$ -ray multiplicities without destroying the good fits to the neutron multiplicities and ER measurements. The first possible solution to improve the high-energy  $\gamma$ -ray multiplicities is to introduce a nonstatistical  $\gamma$ -ray source such as bremsstrahlung. Obviously this can improve the calculated  $\gamma$ -ray spectrum, while retaining the good agreement achieved for the neutron multiplicities and ER cross sections. However, the systematics of bremsstrahlung [72,73] combined with the comparatively low bombarding energies used here ( $E_{\text{lab}} < 12$  MeV/nucleon) suggest that neutron-proton bremsstrahlung cross sections cannot account for the large excess observed from  $E_\gamma = 10$  MeV to 20 MeV. Measurements with similar bombarding energies as in the present work [74–77] indicate that bremsstrahlung emission becomes comparable

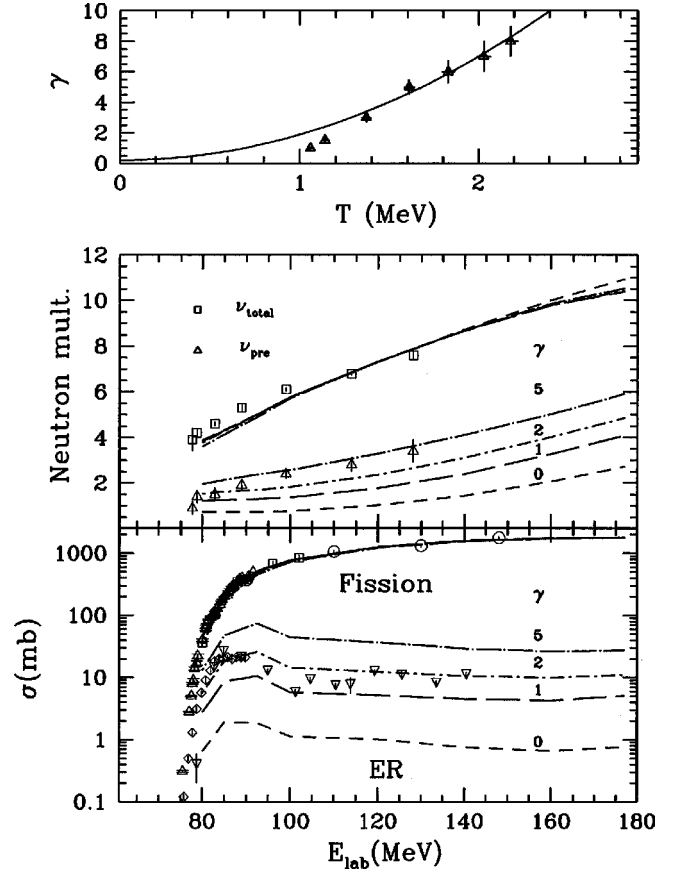


FIG. 9. The same as Fig. 8 now using the Ignatyuk-Reisdorf level density prescription with an added temperature dependence ( $\kappa=0.8$ ).

in magnitude to the statistical components only for  $\gamma$ -ray energies in excess of  $E_\gamma = 20$  MeV. Therefore, we consider it unlikely that bremsstrahlung is the primary source of the excess  $\gamma$  rays observed although we can not rule out the presence of some bremsstrahlung yield for the highest bombarding energies studied.

Another, more realistic approach for fitting the high-energy spectrum is to modify the level density parameter. It has been noticed in earlier works [7–9,12] that the inverse level density parameter had to be increased to describe the high-energy tail of the  $\gamma$  spectra. In the current approach, no such free parameter exists; an arbitrary modification of the radius parameter  $r_0$  in Eq. (12) will adversely affect agreement with nuclear level density data at low energies. As has been discussed in Sec. IV, an additional temperature-dependent factor can be introduced into the Ignatyuk-Reisdorf level density prescription. This method simultaneously retains the good agreement with low-energy level density data while providing some flexibility in the high-energy regime.

We ran a full set of calculations, but now introducing the added temperature dependence of the level density parameter given in Eq. (13) with a strength of  $\kappa=0.8$ . Inspection of the neutron multiplicity and ER fits now reveals a new picture, as seen in Fig. 9. While the neutrons fit quite well with constant  $\gamma=5$  viscosity, the ER show a good fit with  $\gamma=2$ .

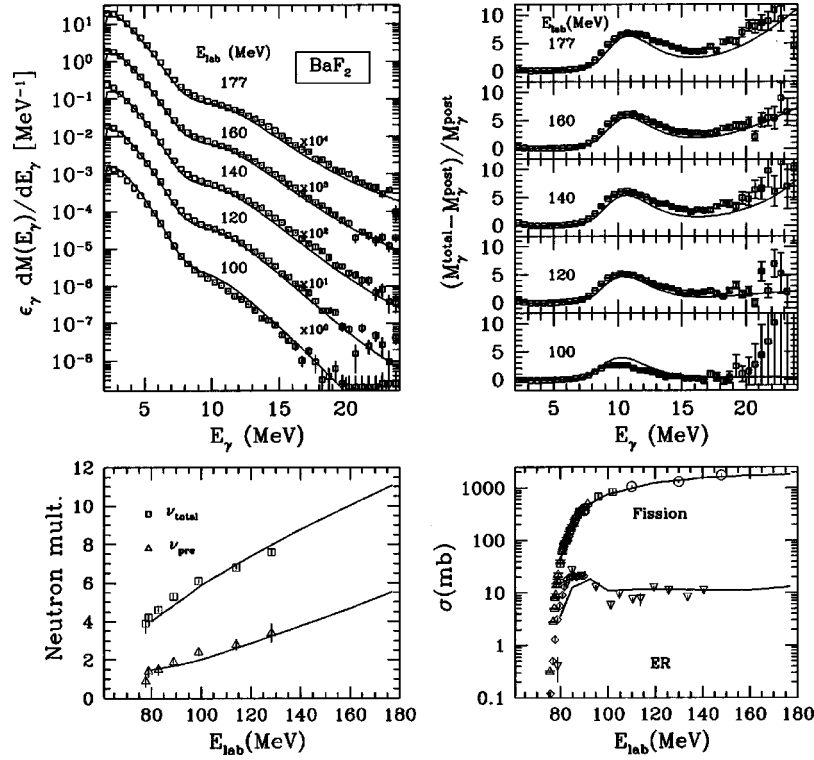


FIG. 10. The same as Fig. 7 now using the temperature-dependent level density according to Eq. (13) and viscosity according to Eq. (16).

The top part of the figure shows the viscosities needed to obtain the best fit for the  $\gamma$ -ray data (not shown here). Now the high-energy tail was nicely fitted, and we observed a weaker temperature dependence:

$$\gamma = 0.2 + 1.7T^2. \quad (16)$$

As a final step we ran calculations for all data with both the temperature-dependent level density parameter according to Eq. (13) and the temperature-dependent viscosity of quadratic dependence. Figure 10 shows the excellent agreement of the data and the calculations.

The temperature dependence of the level density parameter used in these calculations is rather large, decreasing the asymptotic level density parameter from  $\tilde{a} = A/9.6$  at  $T=0$  to  $\tilde{a} = A/12.3$  at  $T=2$  MeV. But it improves dramatically the agreement with the  $\gamma$ -ray data at higher bombarding energies and removes the need to include bremsstrahlung component.

### C. Ignatyuk-Reisdorf approach with deformation dependent nuclear viscosity

Calculations of part B performed with temperature-independent level density parameters (Figs. 7 and 8) demonstrated rather convincingly that a temperature-dependent viscosity was needed in order to bring the calculations into agreement with the data. After introducing the temperature-dependent level densities in order to improve the fit of the high-energy  $\gamma$  spectra the need for a temperature-dependent viscosity becomes less obvious. As was shown in the previous section, the ER cross sections could be fit by a constant viscosity parameter  $\gamma_{\text{fit}}=2$  and the precission neutron mul-

tiplicities are well described by a constant  $\gamma_{\text{fit}}=5$  as well (see Fig. 9). The precission neutron and  $\gamma$  multiplicities have two sources: CN emission behind the saddle before the system has “decided” to fission, and saddle to scission emission. The ER’s, on the other hand, only experience conditions behind the saddle point since by definition they do not pass the saddle.

The difference between the nuclear viscosity experienced by the ER’s and that reflected in the neutron and  $\gamma$ -ray multiplicities suggests the possibility of a scenario along the lines of that proposed by Fröbrich and Gontchar [78–80]. In their original combined dynamical statistical model, nuclear viscosity is determined not by temperature but by the nuclear deformation. Since the CN is in a more compact configuration behind the saddle point (i.e.,  $\beta_{\text{CN}} \approx 0$ ), the ER’s which experience *only* this configuration could reflect a different viscosity than the neutrons or  $\gamma$  rays which are emitted during both stages of the CN decay.

The apparent increase in the nuclear viscosity may also be explained if we suppose different viscosities inside and outside the saddle point. As the bombarding energy is increased, the fusion cross section and thus the average angular momentum of the fused system increases. A significant fraction of the cross section then experiences a low or vanishing fission barrier so that the fast fission process begins strongly to influence the fission process. In consequence the saddle to scission emission gains more importance at higher bombarding energies. Figure 11 shows the Sierk fission barrier, the calculated total cross section, and calculated ER cross section, all as a function of angular momentum. Arrows indicate the angular momentum at which a fast fission cut of  $k=0.5$

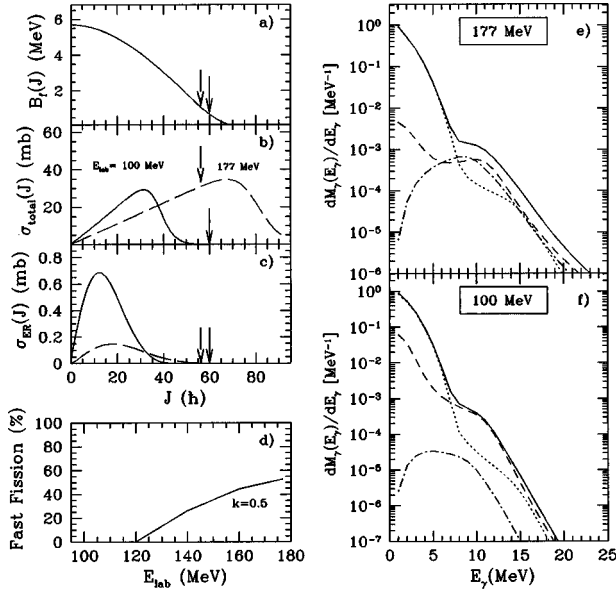


FIG. 11. Calculated angular momentum dependent (a) Sierk fission barrier, (b) total cross section, and (c) ER cross section for the  $E_{lab} = 100$  and  $177$  MeV beam energies. Arrows in panel (a) indicate the angular momenta at which a fast fission cut of  $k=0.5$  ( $E_f T < k$ ) occurs for  $T_{CN} = 1.37$  MeV (solid) and  $T_{CN} = 2.18$  MeV (dashed). Panel (d) displays the % of the total cross section which will undergo fast fission for  $k=0.5$ . The right panels display the calculated unfolded  $\gamma$  spectra (full lines), consisting of the pre-saddle (dashed), saddle to scission (dashed-dotted) and postsission (dotted) components.

( $E_f/T < k$ ) is applied in the CASCADE calculation for  $T_{CN} = 1.37$  MeV and  $T_{CN} = 2.18$  MeV, corresponding to  $E_{lab} = 100$  and  $177$  MeV bombarding energies, respectively. The right panels show the corresponding calculated  $\gamma$  spectra. Whereas for the  $100$  MeV bombarding energy the pre-scission  $\gamma$  decay is dominated by the pre-saddle emission, at  $177$  MeV the pre-saddle and saddle to scission emission have equal probability. Panel (d) of Fig. 11 displays the fast-fission fraction of total cross section for two values of  $k$ . For  $E_{lab} = 100$  MeV, no fast fission occurs since the cut is higher than the maximum angular momentum for both  $k=0.5$  and  $k=1$ . For  $E_{lab} = 177$  MeV, however, 50% of the cross section undergoes fast fission for  $k=0.5$ . It was observed in earlier papers [7,8], that the  $\gamma$ -fission angular correlations do not change significantly with the bombarding energy. The fast fission process affects the  $\gamma$  emission in a special way: the saddle to scission deformation has larger deformation, influencing the energy split in the GDR emission. However, the GDR emitted outside the saddle is mostly emitted in the first few decay steps, before the system cools down during the saddle to scission emission, and the deformation reflected in the GDR is close to the saddle-point deformation. In case of high fissility the saddle-point shape is rather compact. With the increasing bombarding energy the fast fission process takes over, saturating the angular correlation.

If the nuclear viscosity is different inside and outside the saddle point, the measured  $\gamma$  and particle spectra will greatly depend on the fraction of the cross section where fast fission

occurs. On the other hand, the ER's are not affected by the fast fission cut ( $k < 1$ ) due to their much lower average angular momentum.

Figure 12 compares the experimental  $\gamma$  and neutron multiplicities, and ER cross sections to a series of calculations using the same model parameters as in Fig. 9 but now setting the viscosity inside the saddle to  $\gamma_i = 2$  and outside the saddle to  $\gamma_0 = 10$ . As expected, the agreement with the ER cross sections is completely unchanged from Fig. 9. The neutron multiplicities, on the other hand, are now well described within this temperature-independent viscosity prescription. The calculated  $\gamma$ -ray multiplicity spectra fits are equally described by this approach as they were using temperature-dependent viscosities.

## VI. DISCUSSION

The experimental data presented here confirmed the previously observed large increase of the GDR  $\gamma$ -ray yield over the statistical model with the bombarding energy, now over a wider temperature range of  $T = 1.0 - 2.2$  MeV. Fitting the  $\gamma$ -ray multiplicities on an absolute scale provided a very serious constraint on the fit parameters. Following the previous attempt [12] we simultaneously fitted the available neutron multiplicities and ER cross sections as well for this reaction. This global fit demonstrates unambiguously that the experimental  $\gamma$  spectra can be fitted only including large nuclear dissipation.

The detailed calculations revealed that the ER cross sections can not be fitted with the traditional level density approach implemented in CASCADE, the interpolation region produces an unnatural behavior of the fission width. Therefore, we had to use the Ignatyuk-Reisdorf level density approximation, which provides a smooth function of the level density parameter with the temperature. Remarkably we needed a strong temperature dependence of the level density parameter such as predicted by Shlomo and Natowitz [62] in order to explain the high-energy tail of the  $\gamma$  spectra. The observed temperature dependence is even stronger than they predict, and it is in good agreement with the experimental results from charged particle emission [81]. Although the observed temperature dependence of the level density parameter is very strong, it is not unreasonable and the inverse level density parameter is still below the Fermi-gas value. Using this approximation we were able to fit simultaneously all the available  $\gamma$ -ray, neutron multiplicity and ER data for the  $^{16}\text{O} + ^{208}\text{Pb}$  reaction. We observed a large nuclear viscosity  $\gamma$  which is increasing with the bombarding energy.

A recent paper [82] states that all previous works involving the statistical model may have incorrectly calculated fission rates by neglecting a proper handling of the rotational degrees of freedom of compound nuclei. Reference [82] states that calculations including a proposed handling of the nuclear orientation reproduce ER and fission cross sections and pre-scission neutron multiplicities from O-induced reactions *without* the use of strong nuclear dissipation. We note, however, that these calculations rely not only on a modified fission rate formula, but also on a novel temperature-dependent prescription for the nuclear potential energy sur-

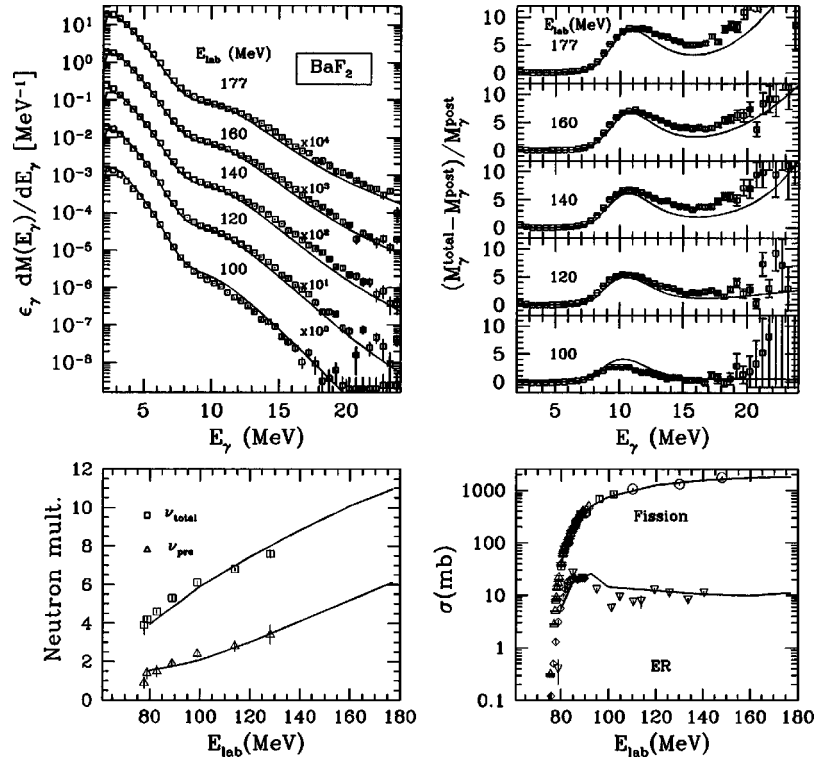


FIG. 12.  $^{16}\text{O}+^{208}\text{Pb}$   $\gamma$  and neutron multiplicities, and ER cross sections compared to calculation with Ignatyuk-Reisdorf level density prescription and additional temperature dependence ( $\kappa=0.8$ ). Nuclear viscosities are constant  $\gamma_i=2$  inside the saddle and  $\gamma_0=10$  outside the saddle point.

face which results in fission barriers that can increase or decrease as a function of temperature. Figs. 1 and 5 of Ref. [82] reveal that without this added temperature dependence the proposed prescription fails to describe the data. CASCADE calculations using fission rates modified according to Eq. (8) of Ref. [82] reveal a similar trend: while the modifications decrease the fission width, they fail to reproduce the data unless the fission barrier is modified or nuclear dissipation is included. The ramifications of this proposal for the present work appear to be minor. Within the model presented in Sec. IV, inclusion of the proposed modified fission rates would somewhat reduce the absolute value of the viscosity parameter but not the overall trends drawn from the present analysis.

Since the increase in bombarding energy simultaneously increases the temperature and also the average angular momentum of the  $^{224}\text{Th}$  system, the exact dependence of the viscosity on either the temperature or on the deformation of the system cannot be unambiguously determined. We could fit the data with two different nuclear viscosity functions: (i) A viscosity increasing with  $T^2$ . This strong temperature dependence would indicate two-body dissipation and is consistent with the volume dissipation of a Fermi liquid. The viscosity does not saturate within the measured temperature range. This is reasonable, as most calculation predict that saturation of the viscosity of the Fermi liquid should not be reached below a temperature of 3–4 MeV. On the other hand, it is not clear from simple dimensional considerations, that a hot  $^{224}\text{Th}$  nucleus would show pure volume dissipation

effects. (ii) Deformation-dependent viscosity  $\gamma(\beta)$ . We fitted the data with constant  $\gamma_i=2$  inside the saddle, and constant  $\gamma_o=10$  outside the saddle, that is during the saddle to scission motion. This type of deformation dependence would suggest one-body dissipation mechanism.

The extraction of the reduced nuclear dissipation coefficient  $\beta=2\omega_0\gamma$  from the determined saddle to scission time requires the precise knowledge of the curvature of the fission barrier (described by the frequency  $\omega_0$ ) and the  $\tau_{\text{ssc}}^0$  saddle to scission time for nonviscous saddle to scission motion. Although these are angular momentum and temperature dependent quantities,  $\tau_{\text{ssc}}^0$  can be determined as  $3.0 \times 10^{-21}$  s with relatively small error.

In the present system  $\gamma$  rays and neutrons are emitted more or less equally inside and outside the saddle point of the hot  $^{224}\text{Th}$  nucleus. In order to differentiate the two possibilities, i.e., a temperature-dependent  $\gamma$  or a deformation dependent  $\gamma$ , this system should be studied in reactions, which favor emission either inside, or outside of the saddle. The saddle-point shape of the nucleus becomes more compact with increasing fissility. Also with increasing nuclear temperature the fast fission process takes over, therefore in heavy, fissile systems with large angular momenta the pre-scission particle and  $\gamma$  emission occurs mostly outside the saddle. This allows the measurement of the viscosity at approximately constant deformation, as a function of temperature. The  $^{32}\text{S}+^{208}\text{Pb}$  system is presently being studied along these lines.

## ACKNOWLEDGMENTS

The authors acknowledge the staff of the Nuclear Structure Laboratory in Stony Brook for providing excellent beams and making the targets. This work was supported in part by the U.S. National Science Foundation.

## APPENDIX

The conclusions of the present paper are dependent on the detailed model calculations including various assumptions about nuclear dissipation. Our model, especially the earlier version of it [7], has been recently criticized in Refs. [51, 52]. That work considered a hot  $^{156}\text{Dy}$  nucleus formed in a fusion reaction, for which the TIMCASC program, developed at KVI Groningen, and the Stony Brook CASCADE calculations yielded very different results. This was blamed on the different time step concept used in the two codes. In the Stony Brook code the time step is defined by the neutron width as

$$\Delta t_\nu = \frac{\hbar}{\Gamma_\nu(E, J)}, \quad (\text{A1})$$

whereas in TIMCASC the full decay width was used to define the time step:

$$\Delta t_{\text{total}} = \frac{\hbar}{(\Gamma_\nu + \Gamma_p + \Gamma_\alpha + \Gamma_f)}. \quad (\text{A2})$$

To examine the difference we introduced the KVI time concept into our code, and did detailed calculations with both methods. Figure 13 shows the results. As one expects, the KVI method produces shorter time steps, especially for the later decay steps, where the fission width becomes larger than the neutron width. However, the size of the time step is important only in the first four steps, before the  $x_h$  fission buildup time saturates. [The saturation point is marked by an arrow on panel (b).] After that the stationary, i.e., *time-independent* fission width has been reached, and the time step size plays no role in the further calculation. The fission and neutron widths still change with the excitation energy, but the time of each step does not change the branching ratios between the decay channels. However, before the stationary fission phase has been reached, the neutron width is much larger than the fission width, so the two time-step approximations are equally good in describing the fission buildup curve [see Eq. (8)]. When the fission widths becomes large enough to play a role ( $10^{-19}$  s in the present case) the stationary phase is already reached. The scenario changes only slightly for a small viscosity: in this case the fission width becomes large, but the  $\tau_f$  fission buildup delay time becomes short. Equation (9) shows that  $\tau_f$  is proportional to the viscosity, and the stationary phase is reached basically in one step.

In general we can state that for large viscosity ( $\gamma > 1$ ) (always the case in the present paper), both approaches yield equal results. Calculations with both methods implemented

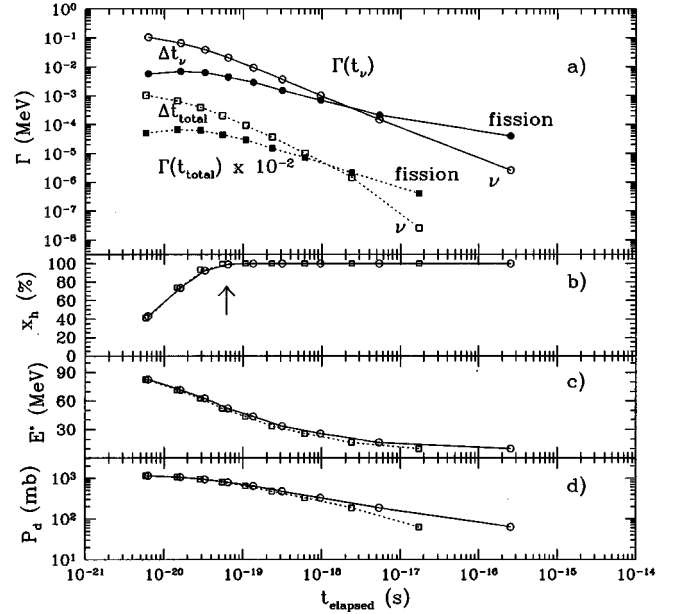


FIG. 13. Comparison of calculations using two definitions for the elapsed time step,  $\Delta t_\nu$  (circles) and  $\Delta t_{\text{total}}$  (squares), for 140 MeV  $^{16}\text{O} + ^{208}\text{Pb}$ . Panel (a) displays the neutron (open symbols) and fission widths (solid symbols), (b) the hindrance factor  $x_h$ , (c) the excitation energy  $E^*$ , and (d) the calculated daughter population  $P_d$  transferred to the next time step, all plotted as a function of the elapsed time.

in our code did not differ by more than 1%. However, for small viscosity ( $\gamma \ll 1$ ) the time step calculated with the full decay width may be better.

The other difference mentioned in Refs. [51,52] is that the fission delay time  $\tau_d$  was calculated for the average spin in the Stony Brook code, whereas in TIMCASC it is calculated for each  $(E, J)$  matrix element. In our present code we introduced this change and calculated  $\tau_f$  for each  $(E, J)$  matrix element. However, the arguments of the previous paragraphs apply again: the difference in handling the transients has only a secondary effect on the process, as it is dominated by the stationary phase.

The two codes are based on the same formalism, outlined in Sec. IV of the present paper. However, the implementation of the model into computer codes is completely different: the Stony Brook method starts with the highly excited CN, and the bookkeeping of the matrices follows the system as it cools down, then to the saddle to scission decay, and finally the fission fragment decay. In TIMCASC the calculation starts from a large fission spectrum data base, and moves backwards in time from the scission point, calculating the presaddle and saddle to scission processes together, as it arrives back at the CN.

Although the underlying physical model is the same, the results of the two codes for  $^{156}\text{Dy}$  were very different. With the Stony Brook code a large viscosity ( $\gamma = 5-10$ ) was needed to describe the data, whereas in TIMCASC a very small viscosity,  $\gamma = 0.01$  (corresponding to 1% change in the fission width) sufficed to describe the  $\gamma$  spectra. In TIMCASC the introduction of this very small viscosity increased the precision  $\gamma$  emission by an order of magnitude, then fur-

ther increase up to  $\gamma=4$  (corresponding to 88% change in the fission width) did not change the spectra noticeably. In a very simple approximation the decrease in the normalized fission widths is equal to the increase of the normalized particle and  $\gamma$  width, similarly the change in the saddle to scission

ion time scales with the saddle to scission emission, thus the total prescission emission scales with viscosity parameter  $\gamma$ . The observed order of magnitude change in the prescission  $\gamma$  yield in TIMCASC with negligible change in the viscosity parameter appears unphysical.

- 
- [1] P. Hänggi, P. Talkner, and M. Borkovec, *Rev. Mod. Phys.* **62**, 251 (1990).
- [2] H. A. Kramers, *Physica (Amsterdam)* **7**, 284 (1940).
- [3] N. Bohr and J. A. Wheeler, *Phys. Rev.* **56**, 426 (1939).
- [4] L. C. Vaz, D. Logan, E. Duck, J. M. Alexander, M. F. Rivet, M. S. Zisman, M. Kaplan, and J. W. Ball, *Z. Phys. A* **315**, 169 (1984); also see, N. N. Ajitanand *et al.*, *ibid.* **316**, 169 (1984).
- [5] D. J. Hinde, R. J. Charity, G. S. Foote, J. R. Leigh, J. O. Newton, S. Ogaza, and A. Chatterjee, *Phys. Rev. Lett.* **52**, 986 (1984).
- [6] M. Thoennessen, D. R. Chakrabarty, M. G. Herman, R. Butsch, and P. Paul, *Phys. Rev. Lett.* **59**, 2860 (1987).
- [7] R. Butsch, D. J. Hofman, C. P. Montoya, P. Paul, and M. Thoennessen, *Phys. Rev. C* **44**, 1515 (1991).
- [8] I. Diószegi, D. J. Hofman, C. P. Montoya, S. Schadmand, and P. Paul, *Phys. Rev. C* **46**, 627 (1992).
- [9] D. J. Hofman, B. B. Back, I. Diószegi, C. P. Montoya, S. Schadmand, R. Varma, and P. Paul, *Phys. Rev. Lett.* **72**, 470 (1994).
- [10] D. Hilscher and H. Rossner, *Ann. Phys. (Paris)* **17**, 471 (1992).
- [11] P. Paul and M. Thoennessen, *Annu. Rev. Nucl. Sci.* **44**, 65 (1994).
- [12] D. J. Hofman, B. B. Back, and P. Paul, *Phys. Rev. C* **51**, 2597 (1995).
- [13] J. Blocki, Y. Boneh, J. R. Nix, J. Randrup, M. Robel, A. J. Sierk, and W. J. Swiatecki, *Ann. Phys. (N.Y.)* **113**, 330 (1978).
- [14] K. T. R. Davies, A. J. Sierk, and J. R. Nix, *Phys. Rev. C* **13**, 2385 (1976); A. J. Sierk and J. R. Nix, *ibid.* **21**, 982 (1980).
- [15] W. R. Abel, A. C. Anderson, and J. C. Wheatley, *Phys. Rev. Lett.* **17**, 74 (1966).
- [16] K.-T. Brinkmann, A. L. Caraley, B. J. Fineman, N. Gan, J. Velkovska, and R. L. McGrath, *Phys. Rev. C* **50**, 309 (1994).
- [17] C. R. Morton, D. J. Hinde, J. R. Leigh, J. P. Lestone, M. Dasgupta, J. C. Mein, J. O. Newton, and H. Timmers, *Phys. Rev. C* **52**, 243 (1995).
- [18] F. Videbaek, R. B. Goldstein, L. Grodzins, S. G. Steadman, T. A. Belote, and J. D. Garrett, *Phys. Rev. C* **15**, 954 (1977).
- [19] B. B. Back, R. R. Betts, J. E. Gindler, B. D. Wilkins, S. Saini, M. B. Tsang, C. K. Gelbke, W. G. Lynch, M. A. McMahan, and P. A. Baisden, *Phys. Rev. C* **32**, 195 (1985).
- [20] D. R. Chakrabarty, S. Sen, M. Thoennessen, N. Alamanos, P. Paul, R. Schicker, J. Stachel, and J. J. Gaardhøje, *Phys. Rev. C* **36**, 1886 (1987).
- [21] W. J. Kernan, N. Gan, A. L. Caraley, B. J. Fineman, R. L. McGrath, and R. J. Vojtech, *Nucl. Instrum. Methods Phys. Res. A* **313**, 563 (1992).
- [22] P. Schotanus, C. W. E. van Eijk, R. W. Hollander, and J. Pijpelink, *Nucl. Instrum. Methods Phys. Res. A* **238**, 564 (1985).
- [23] K. Wisshak, K. Guber, and F. Käppeler, *Nucl. Instrum. Methods Phys. Res. A* **259**, 583 (1987).
- [24] V. Nanal, B. B. Back, and D. J. Hofman, *Nucl. Instrum. Methods Phys. Res. A* **389**, 430 (1997).
- [25] D. J. Hofman, Ph.D. thesis, State University of New York at Stony Brook, 1994.
- [26] S. Sen, D. R. Chakrabarty, P. Paul, J. Stachel, and M. Thoennessen, *Nucl. Instrum. Methods Phys. Res. A* **264**, 407 (1988).
- [27] N. P. Shaw, Ph.D. thesis, State University of New York at Stony Brook, 1999.
- [28] R. Brun *et al.*, CERN-DD/EE/84-1 (1986).
- [29] R. E. Marrs, E. G. Adelberger, and K. A. Snover, *Phys. Rev. C* **16**, 61 (1977).
- [30] M. T. Collins, S. Manglos, N. R. Roberson, A. M. Sandorfi, and H. R. Weller, *Phys. Rev. C* **26**, 332 (1982).
- [31] R. G. Allas, S. S. Hanna, Luise Meyer-Schützmeister, and R. E. Segel, *Nucl. Phys.* **58**, 122 (1964).
- [32] F. Pühlhofer, *Nucl. Phys.* **A280**, 276 (1977).
- [33] V. E. Viola, K. Kwiatkowski, and M. Walker, *Phys. Rev. C* **31**, 1550 (1985).
- [34] D. J. Hinde, J. R. Leigh, J. J. M. Bokhorst, J. O. Newton, R. L. Walsh, and J. W. Boldeman, *Nucl. Phys.* **A472**, 318 (1987).
- [35] A. J. Sierk, *Phys. Rev. C* **33**, 2039 (1986).
- [36] J. J. Gaardhøje, *Annu. Rev. Nucl. Part. Sci.* **42**, 483 (1992).
- [37] P. Grangé and H. A. Weidenmüller, *Phys. Lett.* **96B**, 26 (1980).
- [38] P. Grangé, Li Jun-Qing, and H. A. Weidenmüller, *Phys. Rev. C* **27**, 2063 (1983).
- [39] H. A. Weidenmüller and Zhang Jing-Shang, *Phys. Rev. C* **29**, 879 (1984).
- [40] P. Grangé, *Nucl. Phys.* **A428**, 37c (1984).
- [41] P. Grangé, S. Hassani, H. A. Weidenmüller, A. Gavron, J. R. Nix, and A. J. Sierk, *Phys. Rev. C* **34**, 209 (1986).
- [42] K. H. Bhatt, P. Grangé, and B. Hiller, *Phys. Rev. C* **33**, 954 (1986).
- [43] D. Wilmore and P. E. Hodgson, *Nucl. Phys.* **55**, 673 (1964).
- [44] J. Rapaport, V. Kulkarni, and R. W. Finlay, *Nucl. Phys.* **A330**, 15 (1979).
- [45] F. G. Perey, *Phys. Rev.* **131**, 745 (1963).
- [46] J. R. Huizenga and G. Igo, *Nucl. Phys.* **29**, 462 (1962).
- [47] Write up CASCADE. Report, KVI Groningen (unpublished).
- [48] J. S. Levinger, *Nuclear Photo-Disintegration* (Oxford University Press, Oxford, 1960).
- [49] W. Dilg, W. Schantl, H. Vonach, and M. Uhl, *Nucl. Phys.* **A217**, 269 (1973).
- [50] R. Butsch, M. Thoennessen, D. R. Chakrabarty, M. G. Herman, and P. Paul, *Phys. Rev. C* **41**, 1530 (1990).
- [51] G. van't Hof, W. H. A. Hesselink, A. J. M. Plompen, J. P. S. van Schagen, M. N. Harakeh, M. Kalantar-Nayestanaki, J. C. S. Bacelar, H. van der Ploeg, I. Diószegi, and A. Kugler, *Phys. Rev. C* **54**, 1515 (1996).



- [52] G. van't Hof, W. H. A. Hesselink, A. J. M. Plompen, J. P. S. van Schagen, M. N. Harakeh, M. Kalantar-Nayestanaki, J. C. S. Bacelar, H. van der Ploeg, I. Diószegi, and A. Kugler, *Nucl. Phys. A* **638**, 613 (1998).
- [53] H. Hofmann and J. R. Nix, *Phys. Lett.* **122B**, 117 (1983).
- [54] J. R. Nix, *Nucl. Phys. A* **130**, 241 (1969).
- [55] M. Kicińska-Habior, K. A. Snover, C. A. Gossett, J. A. Behr, G. Feldman, H. K. Glatzel, J. H. Gundlach, and E. F. Garman, *Phys. Rev. C* **36**, 612 (1987).
- [56] M. Kicińska-Habior, K. A. Snover, J. A. Behr, G. Feldman, C. A. Gossett, and J. H. Gundlach, *Phys. Rev. C* **41**, 2075 (1990).
- [57] A. V. Ignatyuk, G. N. Smirenkin, and A. S. Tishin, *Yad. Fiz.* **21**, 485 (1975) [*Sov. J. Nucl. Phys.* **21**, 255 (1975)].
- [58] W. Reisdorf, *Z. Phys. A* **300**, 227 (1981).
- [59] R. W. Hasse, *Ann. Phys. (N.Y.)* **68**, 377 (1971).
- [60] W. D. Myers and W. J. Swiatecki, *Ann. Phys. (N.Y.)* **84**, 186 (1974).
- [61] R. Charity, *Phys. Rev. C* **53**, 512 (1996).
- [62] S. Shlomo and J. B. Natowitz, *Phys. Rev. C* **44**, 2878 (1991).
- [63] S. Shlomo and J. B. Natowitz, *Phys. Lett. B* **252**, 187 (1990).
- [64] J. N. De, S. Shlomo, and S. K. Samaddar, *Phys. Rev. C* **57**, 1398 (1998).
- [65] B. K. Agrawal, S. K. Samaddar, J. N. De, and S. Shlomo, *Phys. Rev. C* **58**, 3004 (1998).
- [66] J. P. Lestone, *Phys. Rev. C* **52**, 1118 (1995).
- [67] H. Rossner, D. J. Hinde, J. R. Leigh, J. P. Lestone, J. O. Newton, J. X. Wei, and S. Elfström, *Phys. Rev. C* **45**, 719 (1992).
- [68] Gan *et al.* [76] measured absolute  $\gamma$ -ray spectra for  $^{112,124}\text{Sn}$  and observed that CASCADE predictions were systematically low by 20% but no reason for this discrepancy was available at the time.
- [69] M. Bolsterli, E. O. Fiset, J. R. Nix, and J. L. Norton, *Phys. Rev. C* **5**, 1050 (1972).
- [70] N. R. Dagdeviren and H. A. Weidenmüller, *Phys. Lett. B* **186**, 267 (1987).
- [71] H. Hofmann and F. A. Ivanyuk, *Phys. Rev. Lett.* **82**, 4603 (1999).
- [72] H. Nifenecker and J. A. Pinston, *Annu. Rev. Nucl. Sci.* **40**, 113 (1990).
- [73] W. Cassing, V. Metag, U. Mosel, and K. Niita, *Phys. Rep.* **188**, 363 (1990).
- [74] R. J. Vojtech, R. Butsch, V. M. Datar, M. G. Herman, R. L. McGrath, P. Paul, and M. Thoennessen, *Phys. Rev. C* **40**, 2441 (1989).
- [75] C. A. Gossett, J. A. Behr, S. J. Luke, B. T. McLain, D. P. Rosenzweig, K. A. Snover, and W. T. Hering, *Phys. Rev. C* **42**, 1800 (1990).
- [76] N. Gan, K.-T. Brinkmann, A. L. Caraley, B. J. Fineman, W. J. Kernan, R. L. McGrath, and P. Danielewicz, *Phys. Rev. C* **49**, 298 (1994).
- [77] M. P. Kelly, K. A. Snover, J. P. S. van Schagen, M. Kicińska-Habior, and Z. Trznadel, *Phys. Rev. Lett.* **82**, 3404 (1999).
- [78] P. Fröbrich and I. I. Gontchar, *Nucl. Phys. A* **563**, 326 (1993).
- [79] I. Gontchar and L. A. Litnevsky, *Z. Phys. A* **359**, 149 (1997).
- [80] P. Fröbrich and I. I. Gontchar, *Phys. Rep.* **292**, 131 (1998).
- [81] B. J. Fineman, K.-T. Brinkmann, A. L. Caraley, N. Gan, R. L. McGrath, and J. Velkovska, *Phys. Rev. C* **50**, 1991 (1994).
- [82] J. P. Lestone, *Phys. Rev. C* **59**, 1540 (1999).